POLYOXOMETALATES

Open Access
RESEARCH ARTICLE

Polyoxometalate@copper catalyst for electrocatalytic coupling of halo-(hetero)aromatic hydrocarbons and carbon dioxide for synthesis of (hetero)aromatic acid

Teng-Teng Wang[1,§], Cong-Cong Zhao[2,§], Bin Liu[3,§], Shi Ru[1] ✉, Si-Yu Jiang[1], Shu-Jun Zhu[1], Wei-Yao Wang[1], Min Zhang[1], Yong-Kai Deng[1], Yulv Yu[4] ✉, and Dejin Zang[1] ✉

[1] *School of Pharmaceutical Sciences & Institute of Materia Medica, National Key Laboratory of Advanced Drug Delivery System, Key Laboratory for Biotechnology Drugs of National Health Commission (Shandong Academy of Medical Sciences), Key Lab for Rare & Uncommon Diseases of Shandong Province, Shandong First Medical University & Shandong Academy of Medical Sciences, Jinan 250117, China*

[2] *Department of Mathematics and Physics, Hebei University of Architecture, Zhangjiakou 075024, China*

[3] *The Third affiliated Hospital of Shandong First Medical University & Affiliated Hospital of Shandong Academy of Medical Science, Jinan 250031, China*

[4] *Chambroad Institute, Binzhou 256500, China*

[§] *Teng-Teng Wang, Cong-Cong Zhao, and Bin Liu contributed equally to this work.*

Cite This: *Polyoxometalates*, **2026**, *5*, 9140126

Read Online

ABSTRACT: Carbon dioxide (CO_2) is an abundant, nontoxic C1 feedstock, and (hetero)aromatic carboxylic acids are crucial structural frameworks and synthetic precursors in organic, materials, and medicinal chemistry. In this study, we present the deposition of a polyoxometalate@copper (SiW_{12}@Cu NP) catalyst on copper foam via a simple electrodeposition method (potential range: 0.6 to −0.8 V; scan rate: 50 $mV \cdot s^{-1}$) for the electrocatalytic carboxylation of halo-(hetero)aromatic hydrocarbons with CO_2. The composite electrode leverages the synergistic effects of SiW_{12} (redox stability, Lewis acidity) and Cu nanoparticles (multivalent states, high conductivity), enhancing electron transfer and CO_2 activation. Under mild reaction conditions (room temperature, 1 atm CO_2, and the absence of noble metals), the prepared catalytic system enables direct carboxylation of not only arenes but also electron-deficient (hetero)arenes, such as halopyridines, with CO_2, achieving a target product yield of over 65% in merely 40 min at a current density of 20 mA. Mechanistic studies confirm that the reaction is initiated by substrate electroreduction, followed by CO_2 fixation. This strategy simplifies the modification of drug intermediates, avoids structural damage to sensitive molecules, and optimizes drug properties through post-carboxylation, providing sustainable technical support for innovation in medicinal chemistry.

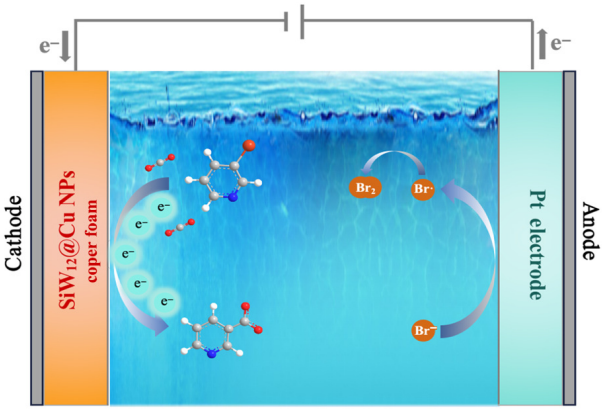

KEYWORDS: polyoxometalate, electrochemical carboxylation, CO_2 conversion, (hetero)aromatic acid synthesis

1 Introduction

Carbon dioxide (CO_2) is a nontoxic and abundant carbon-based raw material with essential applications in the domain of synthetic chemistry [1–4]. In particular, it can be used as a C1 building block in the synthesis of organic compounds, thereby facilitating carbon cycling and meeting the requirements of modern green chemistry [5]. Consequently, the transformation of CO_2 into valuable chemical compounds in a sustainable and environmentally responsible manner represents a green technological approach to carbon recycling [6, 7]. (Hetero)aromatic carboxylic acids are pivotal skeletal structures and significant synthetic precursors within the fields of organic, materials, and medicinal chemistry [8–11]. Consequently, they possess considerable practical applications and have attracted extensive attention [12]. In recent years, significant progress has been made in the carboxylation of (hetero)aromatic hydrocarbons using CO_2 as a raw material. However, metal catalysts are indispensable in such conversion processes. The poor stability of metal–organic catalysts in reactions, difficulties in catalyst recovery, high usage costs [13], the high

Received: November 28, 2025; **Revised:** January 26, 2026
Accepted: February 21, 2026

✉Address correspondence to Shi Ru, curiousrss@163.com; Yulv Yu, yulv.yu@chambroad.com; Dejin Zang, zangdejin_lm@163.com

https://doi.org/10.26599/POM.2026.9140126

activation energy of CO_2 [14], and the need for expensive or toxic metals as sacrificial reducing agents [15, 16] limit the further advancement of this technology to a certain extent. In the pharmaceutical industry, permissible standards for residual metals in synthetic samples are extremely strict. Despite the subsequent development of transition-metal/photoredox synergistic catalytic systems [17], photocatalytic technology still encounters fundamental challenges, including a high photosensitizer cost, low quantum efficiency, and limited light absorption range. Therefore, it is imperative to develop a methodology for the direct, efficient, and highly selective CO_2 carboxylation reaction of (hetero)aromatic hydrocarbons under mild conditions, without the need for costly metal catalysts, ligands, sacrificial reducing agents, or bases.

The advent of electrochemical technology has precipitated the emergence of electrocatalytic organic synthesis as a sustainable and selective alternative to classical organic synthesis, thereby rendering it a focus of attention [18]. Electrochemical organic synthesis has been attracting increasing attention, and electrochemical carboxylation has become one of the most sustainable and efficient methods for the fixation of CO_2 into organic compounds [19–21]. Notable examples include the integration of transition metals with electrochemistry without the use of quantitative reducing agents and electrochemistry-mediated carboxylation of carbon–halogen bonds promoted by organic reducing media. Compared with other areas of research, there is a paucity of literature concerning the carboxylation of electron-deficient (hetero)aromatic compounds driven by electrolysis. Carboxylic acid compounds containing (hetero)aromatic ring structures are ubiquitous in various bioactive compounds, ligands, and functional materials [22]. Among these, nicotinic acid exhibits profound and unique effects on lipid metabolism and is therefore referred to as a "broad-spectrum lipid drug" [23–25]. Accordingly, exploration of electrochemical (hetero)aromatic hydrocarbon carboxylation reactions is of considerble value for CO_2 recycling and for the efficient synthesis of bioactive molecules and drug precursors.

Polyoxometalates (POMs) are a distinct class of structurally defined, molecular-level metal oxide clusters with a broad range of applications in domains such as medicine, catalysis, and materials science [26–42]. POMs exhibit redox stability, multistep redox capability, and ideal ionic conductivity, which enable them to efficiently mediate electron transfer and stabilize reaction intermediates—key functions that promote CO_2 activation when combined with the high conductivity and multivalent states of Cu nanoparticles (NPs) [43]. These characteristics render POMs highly promising electrocatalytic material [44, 45]. As a class of multianionic compounds, POMs can induce the formation of specific morphologies while stabilizing the generated inorganic NPs or organic–inorganic assemblies on the corresponding surfaces. Furthermore, POMs can be modified with different materials, rendering them ideal precursor platforms for the subsequent preparation of new composite materials [46–51]. Overall, POMs constitute an excellent class of functional materials that efficiently mediate electron transfer [45], stabilize reaction intermediates, and optimize electrocatalytic efficiency.

In this study, Cu NPs modified with Keggin-type POM $H_4SiW_{12}O_{40}$ (abbr. SiW_{12}) were deposited on the surface of a copper foam (CF) substrate to prepare a working electrode for electrochemical carboxylation reactions. CF is a substrate material widely used in electrochemical reactions because of its three-dimensional interconnected porous structure, high specific surface area, excellent conductivity, and good mechanical stability. A simple electrodeposition method was used for loading SiW_{12}@Cu NPs onto the CF surface. This approach enabled efficient, precious metal-free electrochemical activation of electron-deficient (hetero)aromatic hydrocarbons for direct carboxylation reactions. Notably, this electrochemical system supports not only the carboxylation of aromatic hydrocarbons but also enables electron-deficient (hetero)aromatic substrates, such as halogenated pyridines, to undergo direct CO_2 carboxylation under mild conditions. The primary benefits of this approach are as follows: (a) the noninvolvement of precious metal catalysts; (b) an environmentally friendly and mild electrochemical strategy that employs low-cost, readily available electrodes and does not involve the use of an anode or alkali; (c) enhanced electron transfer and CO_2 activation kinetics arising from synergistic effects within the composite electrode, which considerbaly improve the efficiency and cycling stability of electrochemical carboxylation reactions. In addition, the preparation process is rendered more straightforward. This strategy simplifies the carboxylation modification process of drug intermediates and reduces the risk of structural damage to sensitive drug molecules under conventional harsh conditions. Furthermore, it regulates the water solubility, biological activity, and metabolic stability of drug molecules via post-carboxylation, providing substantial technical support for molecular optimization and innovation in medicinal chemistry.

2 Experimental section

2.1 Materials and equipments

All reagents were commercially purchased and used without further purification. High-resolution field-emission scanning electron microscopy (FESEM) was performed using a Regulus 8100, high-resolution transmission electron microscopy (HRTEM) was carried out using a Talos F200i, and X-ray diffraction (XRD) measurements were conducted using a Smartlab SE. X-ray photoelectron spectroscopy (XPS) was performed using Thermo K-Alpha. Structural characterization was conducted using a BRUKER 800M nuclear magnetic resonance spectroscopy instrument, and high-performance liquid chromatography (Thermo Fisher Ultimate 3000) was used to determine the yields.

2.2 Experimental procedure

2.2.1 Preparation of working electrode

The working electrode was fabricated using CF as the substrate material. A CF sample (20 mm × 10 mm × 1.5 mm) was immersed in 2.5-M HCl for 30 s, followed by ultrasonic cleaning in acetone, anhydrous ethanol, and pure water for 20 min each. A 1.0 M sodium sulfate solution was prepared, to which anhydrous $CuSO_4$ and SiW_{12} were added in varying molar ratios and stirred until clear. The electrochemical setup comprised a standard three-electrode system, with CF, a platinum wire, and a saturated calomel electrode (SCE) serving as the working, counter, and reference electrodes, respectively. The electrochemical experiments were controlled using a Chenhua CHI 760E electrochemical workstation. All experiments were conducted at room temperature (~ 25°C). The electrochemical deposition of the catalyst onto the CF surface was performed using cyclic voltammetry (CV). A 1-cm^2 CF sample was immersed in the solution and continuously scanned for five

cycles at a potential range of 0.6 to −0.8 V at a scan rate of 50 mV·s^{-1}. All potentials in this section are referenced to the SCE. After electrodeposition, the resulting electrode material was sonicated in pure water for 1 min to remove surface impurities. Subsequently, the electrode material was rinsed three times with anhydrous ethanol and pure water and then pumped with N_2 for drying.

2.2.2 Experimental procedure of electrocatalysis (hetero)aromatic hydrocarbon carboxylation

Electrocatalytic reactions were conducted in a 5-mL undivided electrolytic cell, and all experiments were controlled using a DJS-292B potentiostatic apparatus. The prepared electrode served as the working electrode, whereas a platinum wire acted as the counter electrode. Five milliliters of ultradry N,N-dimethylformamide (DMF) was introduced into the electrolytic cell. Halogenated (hetero)aromatic hydrocarbons (0.25 mmol), tetrabutylammonium hexafluorophosphate (Bu_4NPF_6, 0.25 mmol), and 1,5,7-triazabicyclo[4.4.0]dec-5-ene (TBD, 1 mmol) were added to the 5 mL cell equipped with a magnetic stir bar. Subsequently, the assembled cell was purged with CO_2 gas for over 40 min to saturate the system with CO_2. A constant current of 20 mA was applied at room temperature for 40 min, maintaining CO_2 purging throughout the reaction. After the reaction, a 2.5-M hydrochloric acid solution was added to adjust the pH to 3. Subsequently, the mixture was extracted and purified by column chromatography to isolate the target products.

2.3 Computation details

All geometric optimizations and single-point energy calculations were performed using the Vienna *ab initio* simulation package [52, 53]. The generalized gradient approximation with the Perdew–Burke–Ernzerhof [54] exchange correlation function was adopted to describe the exchange correlation interactions, whereas the DFT-D3 method was adopted to accurately account for the van der Waals (vdW) interactions [55]. A plane wave cutoff energy of 400 eV was applied. To reduce interlayer interactions in periodic models, a vacuum spacing of 20 Å was introduced, and the Brillouin zone was sampled at the Γ point only. Convergence thresholds were established at 10^{-4} eV and 0.05 eV/Å for energy and atomic forces, respectively.

The adsorption energy (E_{ads}) [56] was calculated as follows:

$$E_{ads} = E_{A-S} - E_S - E_A$$

where E_{A-S}, E_S, and E_A denote the total energies of the adsorbate–substrate (A–S) complex, substrate (S), and adsorbate (A), respectively.

3 Results and discussion

3.1 Structural characterization of prepared electrode

The preparation of the CF electrodes loaded with SiW_{12}@Cu NPs was accomplished via electrodeposition. Figure 1(a) illustrates the detailed preparation process of SiW_{12}@Cu NPs. FESEM revealed a layer of cubic NPs with diameters of approximately 500 nm deposited on the CF framework (Fig. 1(b)). The addition of various quantities of SiW_{12} resulted in distinct morphological transitions of the NPs, from polyhedron structures (Fig. S1 in the Electronic Supplementary Material (ESM)) to cubic configurations. This crystallization behavior, which is typically observed in static solutions, aligns with previous reports [3, 57], indicating that SiW_{12} exerts a certain degree of control over the catalyst morphology. XRD analysis (Fig. 1(c)) reveals that SiW_{12}@Cu NPs exhibit good crystallinity. The main diffraction angles 2θ = 43.29°, 50.43°, and 74.13° correspond to the (111), (200), and (220) crystal planes of copper, respectively (Cu PDF#000-004-0836). The weaker diffraction peaks at 37.01° and 62.44° correspond to the (111) and (220) crystal planes of Cu_2O, respectively (Cu_2O PDF#000-034-1354). This finding suggests that Cu in SiW_{12}@Cu NPs exists in different valence states, including Cu^0 and Cu^+, thereby demonstrating exceptional redox performance.

Figure 2(a) shows the HRTEM image of the obtained SiW_{12}@Cu NPs, revealing their crystal growth orientation and distinct lattice fringes at interplanar spacings of 0.25, 0.10, and 0.12 nm. These fringes correspond to the Cu_2O (111), (400), and (222) crystal planes, respectively, consistent with the single-crystal XRD pattern dominated by the (111) plane, as shown in Fig. 1(c). In the selected area electron diffraction pattern shown in Fig. 2(b), the diffraction spots exhibit a regular arrangement and can be indexed to the (111), (200), and (100) crystal planes of Cu_2O (along the [1$\bar{1}$0] crystal zone axes). This finding further substantiates the presence of the single-crystal order of the Cu_2O phase within the material. When considered in conjunction with the HRTEM results, these findings indicate that the Cu_2O phase possesses a well-defined crystal zone structure. The energy-dispersive X-ray spectroscopy (EDS) spectra (Figs. 2(c)–2(f)) reveal a uniform distribution of Cu, Si, and W within the NP regions. This result validates the effective loading of SiW_{12} onto the Cu NP surface, thereby forming the SiW_{12}@Cu NP composite material. In combination with XRD analysis, the Cu-based NPs have a polycrystalline structure, which provides a plethora of reactive sites to facilitate CO_2 adsorption and activation. The uniform loading of SiW_{12} modulates the electronic structure of Cu-based NPs and synergistically catalyzes CO_2 conversion reactions through its acidic sites and redox properties. This approach is anticipated to enhance reaction selectivity and activity, thereby providing a structural foundation for the design of highly efficient electrochemical catalysts for the synthesis of organic CO_2.

To evaluate the surface chemical composition and electronic states of the SiW_{12}@Cu NP catalyst, the synthesized materials were analyzed using XPS. The binding energies of 952.30 and 932.60 eV in Fig. 3(a) are ascribed to the Cu $2p_{1/2}$ and Cu $2p_{3/2}$ orbitals of Cu^+, respectively. This finding confirms that Cu exists in the +1 oxidation state as Cu_2O on the catalyst surface. The Cu $2p_{1/2}$ and Cu $2p_{3/2}$ peaks located at 954.60 and 934.60 eV, respectively, together with a weak satellite peak at approximately 945 eV, confirm the presence of a small amount of Cu^{2+} species on the catalyst surface. This phenomenon can be attributed to the excessive oxidation of the catalyst surface when exposed to air. Figure 3(b) shows the corresponding Cu Auger electron spectroscopy (AES). The Cu LMM main peak region of SiW_{12}@Cu NPs is dominated by a deconvoluted peak at 916.50 eV, corresponding to Cu^+, while the peak at 918.25 eV indicates zero-valent copper (Cu^0), with a ratio of Cu^0 to Cu^+ of 0.088. The aforementioned characterization demonstrates that Cu on the catalyst surface exhibits mutliple electronic states, which is beneficial for electrochemical redox reactions by providing multiple active sites. Furthermore, we hypothesize that the interaction between POMs and Cu NPs during electrochemical codeposition involves vdW forces between the

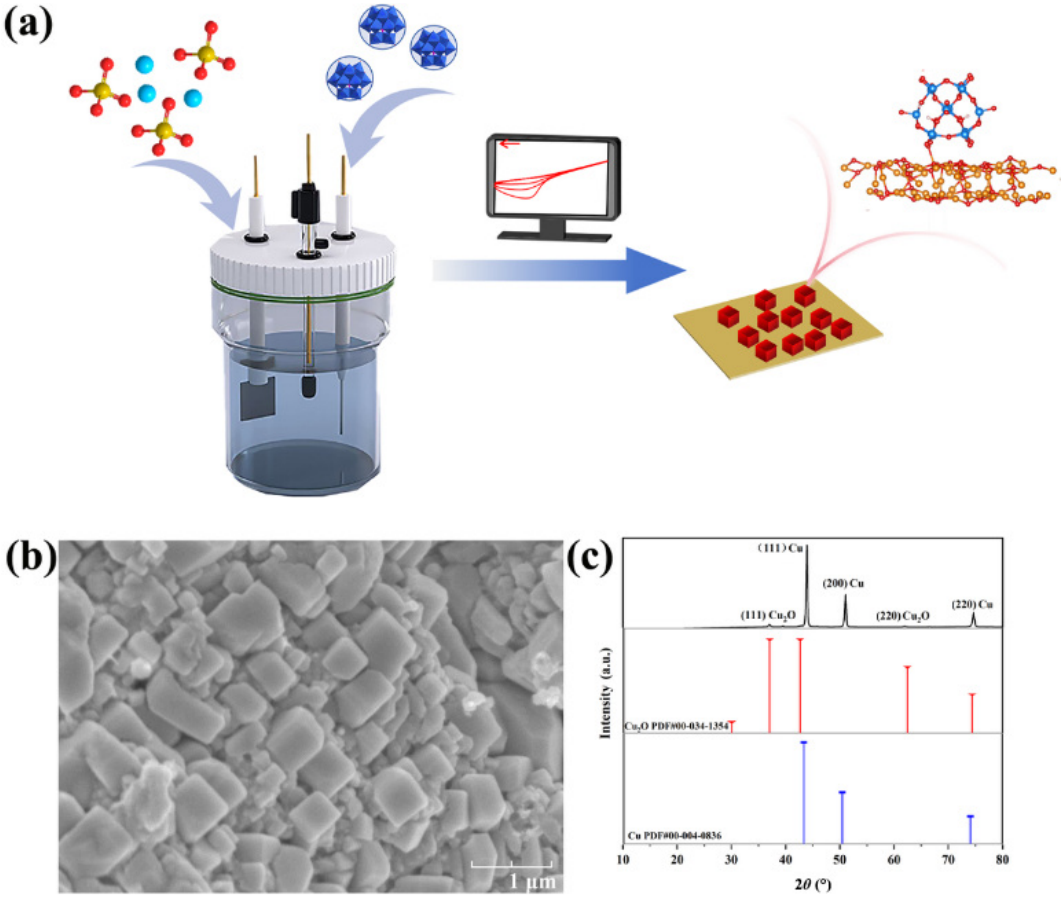

Figure 1 (a) Schematic preparation process of the designed SiW_{12}@Cu NPs. (b) SEM image of the as-obtained SiW_{12}@Cu NPs composite. (c) XRD patterns of Cu (blue curve, PDF#00-004-0836), Cu_2O (red curve, PDF#00-034-1354), and SiW_{12}@Cu NPs (black curve).

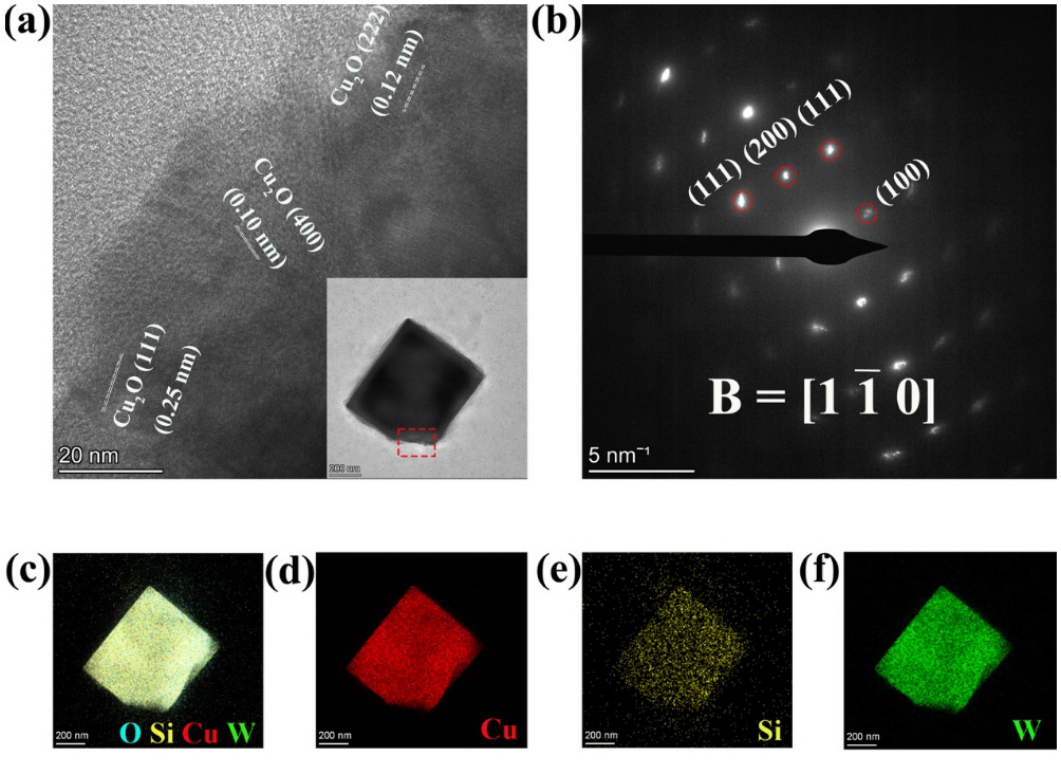

Figure 2 (a) HRTEM image of the selected area of SiW_{12}@Cu NPs. (b) The selected area electron diffraction (SAED) image of SiW_{12}@Cu NPs (B represents the zone axis). (c)–(f) EDS mapping of Cu (red), Si (yellow) and W (green) over SiW_{12}@Cu NPs.

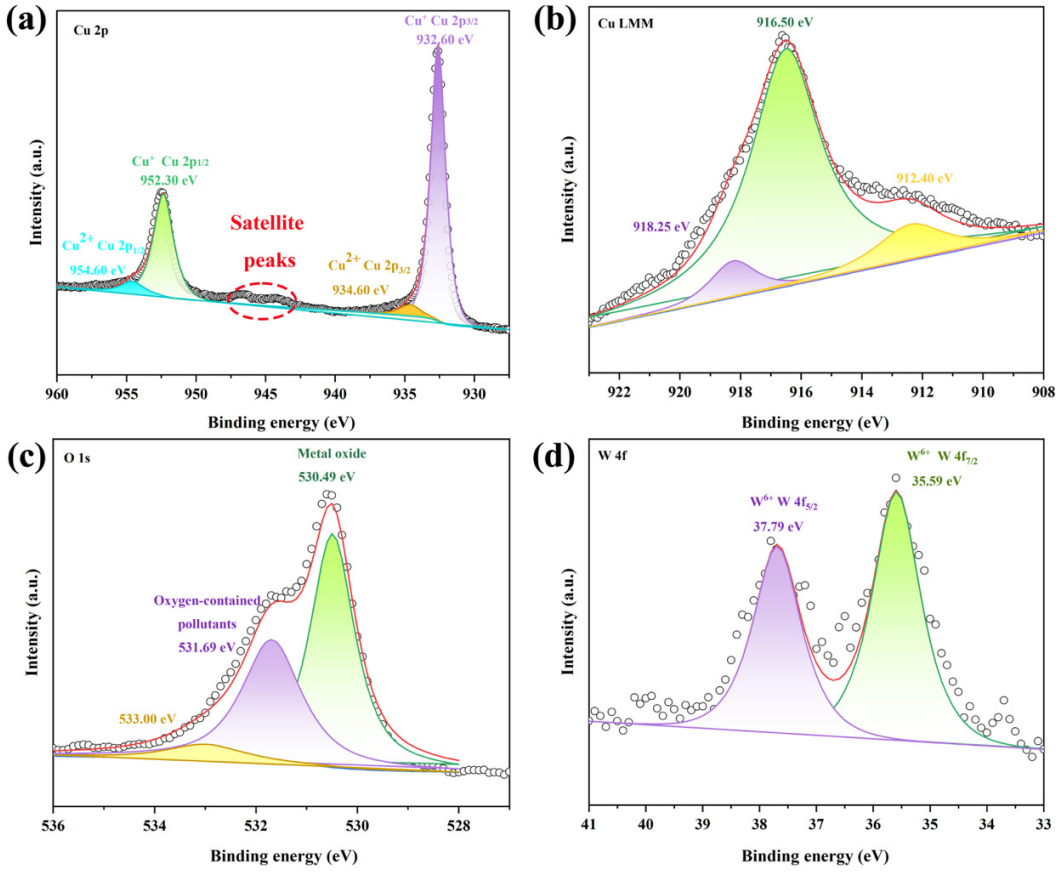

Figure 3 XPS spectra of (a) Cu 2p, (b) Cu LMM, (c) O 1s, and (d) W 4f region in SiW_{12}@Cu NPs.

oxygen atoms in POMs and copper [58, 59]. This process alters the oxidation state of Cu^0, resulting in the formation of a valence distribution where Cu^+ and Cu coexist. This finding suggests that the adsorption of POMs onto the surface of the prepared Cu NPs is not solely reliant on electrostatic interactions but also contingent on the interaction between POMs and Cu NPs [60–62]. When combined with the XPS analysis of O 1s (Fig. 3(c)), after peak fitting, two characteristic oxygen species are identified. The intense maximum at 530.49 eV is attributed to lattice oxygen (O^{2-}) within the metal oxide matrix, whereas the peak at 531.69 eV is attributed to surface-adsorbed oxygen-containing species. These peaks may have originated from hydroxyl (–OH) groups or other oxygen-containing organic/inorganic impurities adsorbed on the material surface. The peak at 533.00 eV corresponds to water molecules adsorbed on the catalyst surface. The W 4f spectrum (Fig. 3(d)) shows characteristic peaks at 35.59 and 37.79 eV, corresponding to the $4f_{7/2}$ and $4f_{5/2}$ orbital signals of W^{6+}, respectively. This finding confirms the existence of W in SiW_{12} in the +6 oxidized state, with minimal valence alterations. Consequently, after composite formation with Cu-based NPs, SiW_{12} maintains its intrinsic redox properties. This result demonstrates that W^{6+} promotes CO_2 activation and polarization through its strong Lewis acidic sites. Concurrently, SiW_{12} provides a stable proton transfer environment for the reaction, thereby synergistically enhancing CO_2 activation and conversion efficiency alongside Cu-based active sites.

3.2 Screening of reaction conditions for electrochemical halogenated (hetero)aromatic hydrocarbon carboxylation

In the preliminary experiments, 3-bromopyridine was used as a model substrate to optimize the reaction conditions, and the reaction was conducted under a CO_2 atmosphere (1 atm). After screening various reaction conditions, we discovered that pyridine-3-carboxylic acid could be synthesized within 40 min with a separation yield of 65.35% in an undivided cell. This was achieved using the prepared SiW_{12}@Cu NPs loaded on CF as the reusable working electrode, Bu_4NPF_6 as the electrolyte, and TBD as the additive in DMF as the solvent at a constant current (20 mA). Control experiments demonstrated that the electrolyte is critical for this conversion process. In the absence of Bu_4NPF_6, the target product was not detected (Table 1, entry 2). In this study, the performance of various electrolytes was evaluated. The results (Table 1, entry 3) demonstrate that Bu_4NPF_6 exhibits superior performance compared with tetrabutylammonium bromide (Bu_4NBr), tetrabutylammonium iodide (Bu_4NI), and cetyltrimethylammonium bromide (CTAB), with respective yields of 54.08%, 22.97%, and 49.42%. In addition, various solvents were evaluated, including DMF, acetonitrile (MeCN), and H_2O (Table 1, entries 4 and 5). The findings suggest that DMF is the optimal solvent for this transformation reaction. Furthermore, various electrode materials were examined, including Pt(–)/Pt(+), CF(–)/Pt(+), SiW_{12}@Cu NPs(+)/Pt(–), Ni Foam(–)/Pt(+), and RVC(–)/Pt(+), which yielded conversion rates of 40.24%, 58.83%, 66.35%, 40.50%, and 5.37%, respectively. The results indicate that the cathode material significantly influences the conversion process, with the CF electrode loaded with SiW_{12}@Cu NPs exhibiting superior performance (Table 1, entries 6–10). Several studies on reaction time and current were conducted (Fig. S2 in the ESM) to determine the optimal conditions for the synthesis of pyridine-3-

Table 1 Optimization of reaction conditions[a]

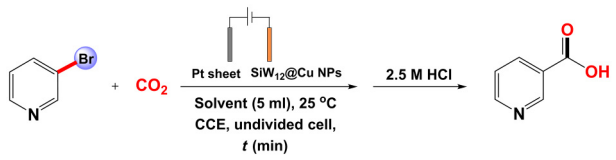

Entry	Alteration	Yield (%)[b]
1	None	65.35
2	W/O Bu_4NPF_6	N.D.
3	Bu_4NBr, Bu_4NI, CTAB instead Bu_4NPF_6	54.08, 22.97, 49.42
4	MeCN as solvent	< 1
5	H_2O as solvent	N.D.
6	Pt(−)/Pt(+)	40.24
7	CF(−)/Pt(+)	58.83
8	SiW_{12}@Cu NPs(+)/Pt(−)	66.35[c]
9	Ni foam(−)/Pt(+)	40.50
10	RVC(−)/Pt(+)	5.37
11	TEA, TPA, DBN, DBU instead TBD	12.40, 11.34, 37.07, 45.11
12	W/O electricity or CO_2	N.D.

[a]Reaction conditions: undivided cell, substrate (0.1 mmol), catalyst ($n(CuSO_4)$:$n(SiW_{12})$= 8:1), Bu_4NPF_6 (1.0 equiv.) in 5 mL solvent, 25 °C, under CO_2, copper foam loaded with SiW_{12}@Cu NPs as the anode, and Pt sheet as the cathode, CCE = 20 mA. N.D. = not detected, MeCN = acetonitrile, DMF = dimethylformamide, TEA = triethylamine, TPA = triphenylamine, TBD = 1,5,7-triazabicyclic[4.4.0]dec-5-ene, DBN = 1,5-diazabicyclo[4,3,0]non-5-ene, DBU = 1,8-diazabicyclo[5,4,0]undec-7-ene; CTAB = N,N,N-trimethyl-1-hexadecanaminium bromide, CCE = constant current electrolysis. [b]Determined by Thermo-Fisher HPLC Ultimate 3000. [c]Anodic dissolution.

carboxylic acid. The results demonstrated that the highest yield of the desired compound (65.35%) was achieved at a current of 20 mA and a substrate concentration of 0.1 mmol. Subsequent comparative experiments demonstrated that the basic organic medium plays a crucial role in the conversion reaction (Table 1, entry 11). Replacing TBD with triethylamine, triphenylamine, 1,5-diazabicyclo[4.3.0]non-5-ene, or 1,8-diazabicyclo[5.4.0]undec-7-ene significantly reduced the reaction efficiency. Subsequent control experiments confirmed that electrical energy and CO_2 are critical factors for the advancement of the reaction. In the absence of either component, no formation of the target product was detected within the system (Table 1, entry 12).

3.3 Substrate scope

With optimized conditions established, we evaluated the generality of the protocol across a diverse range of halogenated (hetero)aromatic substrates (Table 2). The method proved broadly applicable, with yields spanning from 2.43% to > 99%.

For heteroaromatic substrates, reactivity was dictated by electronic effects and substitution patterns. Although 3-iodopyridine afforded a moderate yield (51.46%), the introduction of a fluorine substituent in 2-fluoro-5-bromopyridine increased the yield to > 99%, drastically outperforming its methyl analog (33.5% for 2-methyl-5-bromopyridine). We attribute this enhancement to the strong electron-withdrawing character of fluorine, which shifts electron density away from the C-5 position. This destabilization of the $C_{(5)}$-Py bond facilitates the generation of the reactive 6-fluoropyridine-3-ium intermediate, thereby promoting efficient CO_2 capture.

In sharp contrast, 4-bromopyridine was virtually inert (2.43% yield). CV confirms that this substrate is redox-inactive under standard conditions (Figs. S8–S14 in the ESM), a failure we ascribe to three synergistic factors. First, the substrate suffers from intrinsic instability; the nitrogen atom activates the C-4 position for nucleophilic attack, resulting in rapid intermolecular self-quaternization (polymerization) before the substrate reaches the electrode. Second, even if the radical intermediate forms, resonance delocalization onto the nitrogen atom significantly reduces its nucleophilicity toward CO_2. Finally, the C-4 position is highly susceptible to dimerization, further competing with the desired carboxylation. Conversely, 3-bromopyridine avoids these resonance pitfalls and maintains a sufficient charge density at the metaposition to ensure an effective reaction.

Beyond heterocycles, simple aryl bromides and iodides were highly amenable to this transformation, producing target acids in quantitative yields (> 99%). However, the reaction remained sensitive to electronic effects: The electron-donating groups (e.g., methyl and methoxy) generally impeded the reaction, limiting yields to 25%–51% compared with their electron-deficient counterparts.

3.4 Mechanism research

The incorporation of CO_2 (which is abundant and recyclable) into the synthesis of carboxylic acids provides significant synthetic advantages. These advantages stem from the fact that carboxylic acids and their derivatives serve as common structural units in natural products, drug molecules, and bioactive compounds. To extend the range of application of such electrochemical carboxylation reactions, systematic mechanistic investigations were conducted. Initially, detailed mechanistic studies were conducted using CV (Fig. 4(a)). An irreversible reduction peak for the substrate (3-bromopyridine) was observed at a potential of −1.138 V vs. reversible hydrogen electrode (RHE) (Fig. 4(a), orange curve). CO_2 exhibited an irreversible reduction peak at a potential of −1.369 V (vs. RHE) (Fig. 4(a), green curve). Furthermore, in the presence of the substrate (3-bromopyridine) under a CO_2 atmosphere, a significant shift in the reduction potential of the system was observed (Fig. 4(a), blue curve). The reduction potential exhibited a positive shift, indicating that the reaction can proceed at a lower energy level within the system. This finding suggests a synergistic reduction in the system. 3-Bromopyridine functions as an electron acceptor, undergoing reduction, whereas CO_2 participates as an electrophile, thereby lowering the overall reaction energy barrier. Furthermore, linear sweep voltammetry (LSV) was performed for different substrates (Fig. 4(c)). After normalizing the corresponding current densities to respective electrochemical surface areas (Fig. S3 in the ESM), the curves indicate that the electrochemical reduction degree of 3-bromopyridine is higher than that of CO_2, suggesting that the reaction initiates with the electroreduction of 3-bromopyridine rather than CO_2. Furthermore, the catalytic performance of CF and SiW_{12}@Cu NPs was compared based on LSV (Fig. 4(b)). The LSV curves demonstrate that CF exhibits a broad reduction potential range devoid of distinct characteristic reduction peaks, indicating that the pure CF substrate exhibits weak catalytic activity in this system. In contrast, the SiW_{12}@Cu NP composite exhibits significant reduction currents within the −2 to −1.25-V range, with an earlier

Table 2 Substrate scope[a,b,c]

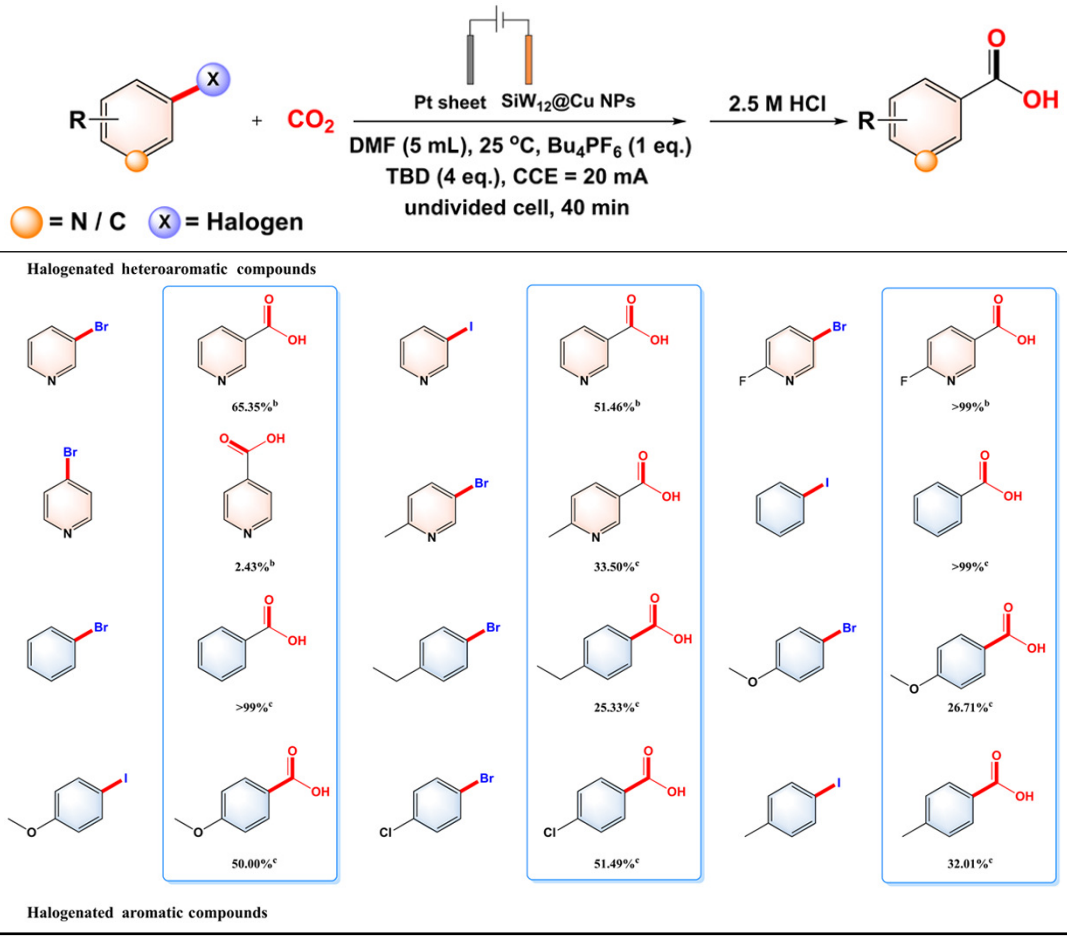

[a]Reaction conditions: undivided cell, substrate (0.1 mmol), catalyst (n($CuSO_4$):n(SiW_{12})= 8:1), Bu_4NPF_6 (1.0 equiv.) in 5 mL solvent, 25 °C, under CO_2, copper foam loaded with SiW_{12}@Cu NPs as the anode, and Pt sheet as the cathode, CCE = 20 mA. N.D. = not detected, MeCN = acetonitrile, DMF = dimethylformamide, TEA = triethylamine, TPA = triphenylamine, TBD = 1,5,7-triazabicyclic[4.4.0]dec-5-ene, DBN = 1,5-diazabicyclo[4,3,0]non-5-ene, DBU = 1,8-diazabicyclo[5,4,0]undec-7-ene; CTAB = N,N,N-trimethyl-1-hexadecanaminium bromide, CCE = constant current electrolysis. [b]Determined by Thermo-Fisher HPLC Ultimate 3000. [c]Anodic dissolution.

onset potential for the reduction reaction. Furthermore, the absolute current density of the composite was considerably higher than that of CF, indicating superior reaction kinetics and faster electron transfer rates.

To investigate the dynamic changes in electrode structure and performance during electrocatalytic processes, electrochemical impedance spectroscopy measurements were performed on the SiW_{12}@Cu NP electrode in different chemical environments. The impedance spectra presented in Figs. 4(d) and 4(e) were collected in a 50-mM Bu_4NPF_6 solution in DMF at 25 °C. At relatively positive potentials ranging from −0.38 to −0.78 V, the impedance arc exhibits a marked increase, suggesting high charge transfer resistance and slow reaction kinetics. When the potential becomes negative, with a range of −0.88 to −1.48 V, a significant shortening of the impedance arc is observed. A comparison of Figs. 4(d) and 4(e) reveals that the impedance arc diameter for the 3-bromopyridine monosubstrate system is markedly larger than that for the cosubstrate system within the same potential range. This finding further corroborates our hypothesis that the addition of CO_2 exerts a synergistic effect, thereby reducing the reaction energy barrier and accelerating electron transfer. This conclusion is consistent with the CV analysis results. As shown in Fig. S4 in the ESM, the Bode phase (θ) plots of SiW_{12}@Cu NP composite electrodes in various chemical environments facilitate further analysis of the impedance characteristics and interfacial processes of the system. As shown in the accompanying figure, the phase angle in the high-potential region (−0.4 to −0.8 V) is significantly less than 90°, indicating high electrochemical reaction resistance (limited charge or mass transfer) and slow reaction kinetics at this particular point. In the low-potential region (−0.9 to −1.5 V), the phase angle in the medium-frequency range gradually increases toward 90°, whereas the peak shifts toward higher frequencies. This finding suggests accelerated charge transfer rates, resulting in more efficient electron transfer to the substrate. Concurrently, the phase angle changes in the low-frequency range reflect optimized mass transfer processes, indicating that the overall reaction has entered a kinetically favorable regime.

To probe the reaction mechanism and the key intermediate of the electrocatalytic carboxylation of 3-bromopyridine, *in situ* electron paramagnetic resonance (EPR) spectroscopy was used to monitor radical intermediates, with 5,5-dimethyl-1-pyrroline-N-oxide (DMPO) as the spin-trapping agent. Figure 5 shows the corresponding spectra.

The spectra display six-peak EPR signals, which are considered

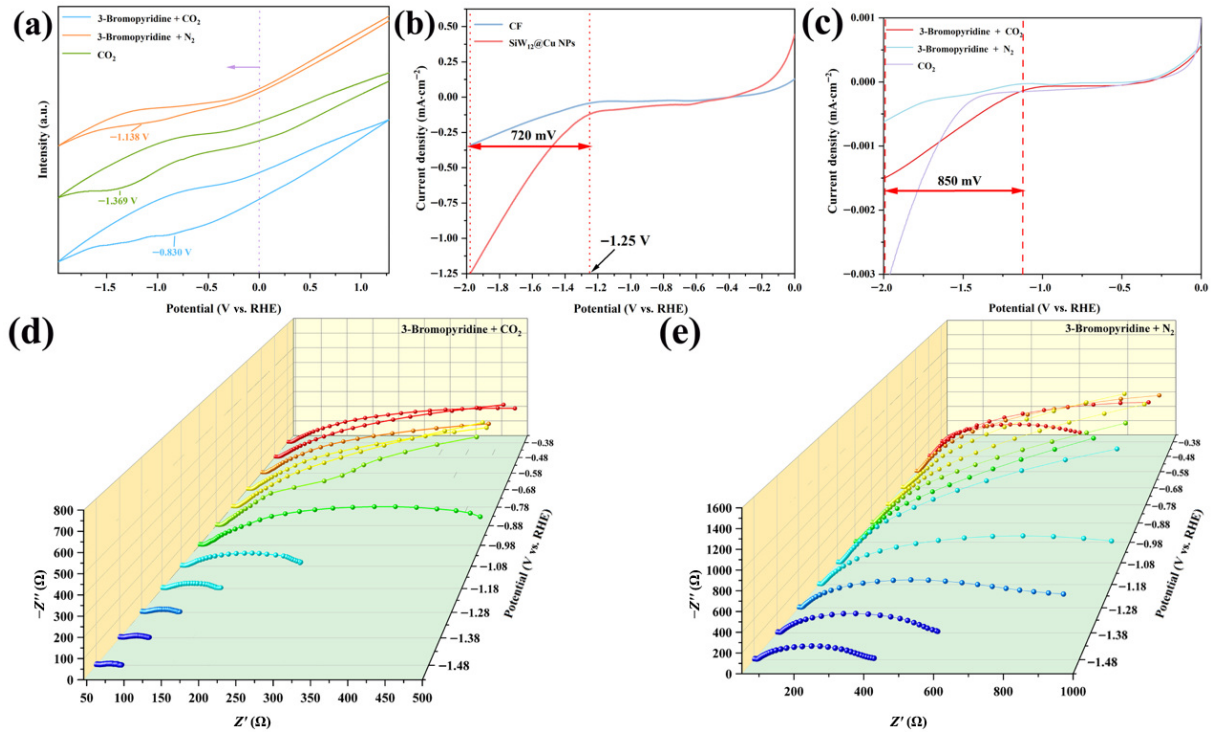

Figure 4 Using SiW_{12}@Cu NPs as work electrode, Pt sheet and Ag/AgCl as counter and reference electrode. Scan rate:100 mV·s^{-1}. Solvent: 0.05 M Bu_4NPF_6 in DMF. (a) CV curves of 3-bromo-pyridine (orange curve), CO_2 (green curve), and 3-bromo-pyridine under CO_2 atmosphere (blue curve). (b) LSVs comparison of Copper Foam (blue curve), and SiW_{12}@Cu NPs (red curve). (c) LSVs comparison of 3-bromo-pyridine (blue curve), CO_2 (purple curve), and 3-bromo-pyridine under CO_2 atmosphere (red curve). EIS of 3-bromopyridine under different potentials in (d) CO_2 and (e) N_2.

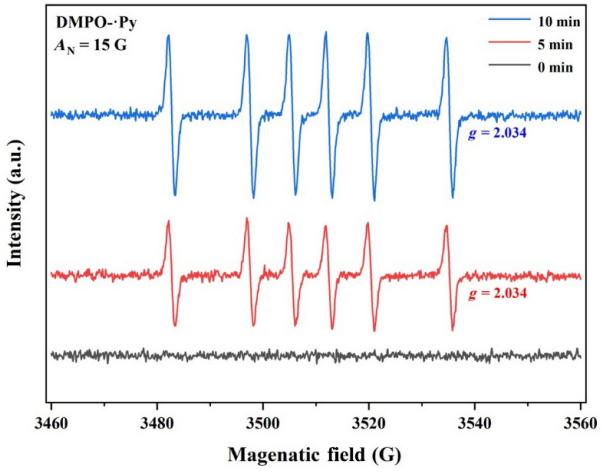

Figure 5 EPR spectra of DMPO-·Py at different reaction times.

DMPO-·Py spin adducts (where ·Py denotes the 3-pyridyl radical) characterized by hyperfine coupling constants A_N = 15 G and a *g*-factor of 2.034. Three sets of spectra correspond to different reaction durations: The black trace (0 min) shows only baseline noise (no radical signal), confirming the absence of pre-existing radicals in the initial system. Upon initiation of the electrocatalysis process, distinct EPR signals emerge: The red trace (5 min) exhibits a well-resolved radical adduct signal, and the blue trace (10 min) exhibits a further enhanced signal intensity. These results directly demonstrate that the 3-pyridyl radical (·Py) is generated as a key intermediate during the electrocatalytic dehalogenation of 3-bromopyridine, and its concentration increases with prolonged electrolysis time. This observation provides critical spectroscopic evidence for the proposed radical pathway in the dehalogenative carboxylation reaction.

In research related to electrode materials, controlling the surface electron confinement distribution of electrode materials plays a dominant role in improving the electrochemical behavior of the materials. In this study, to elucidate the origin of the improved electrochemical performance, we performed density functional theory (DFT) calculations on the SiW_{12}@Cu_2O interface. The optimized structural model reveals that the SiW_{12} cluster is anchored onto the Cu_2O surface through a stable W–O_t–Cu bridge with a calculated bond length of 2.36 Å, indicating robust chemical integration rather than simple physical adsorption (Figs. 6(a) and 6(b)).

Crucially, charge density difference (CDD) analysis provides visual evidence of significant interfacial electron redistribution (Fig. 6(c)). Bader charge analysis reveals a directional electron transfer of 0.46*e* from the Cu_2O substrate to the SiW_{12} cluster [63, 64]. As shown in the CDD map, the electron depletion regions (cyan) are concentrated on the interfacial Cu atoms, whereas the electron accumulation regions (yellow) are localized on the POM framework. This modulation of the microscopic electronic structure establishes a highly efficient synergistic catalytic platform for the electrocatalytic carboxylation of 3-bromopyridine to synthesize nicotinic acid (Vitamin B3). The mechanistic advantages are primarily manifested in the following three aspects:

1. Electronic activation via SiW_{12} clusters

First, the electron-enriched SiW_{12} clusters (indicated by the yellow regions in the figure) serve as potent "electron pumps" and active reduction centers. This function aligns with the classic "electron sponge" property of Keggin-type POMs, which can reversibly accept multiple electrons while maintaining structural

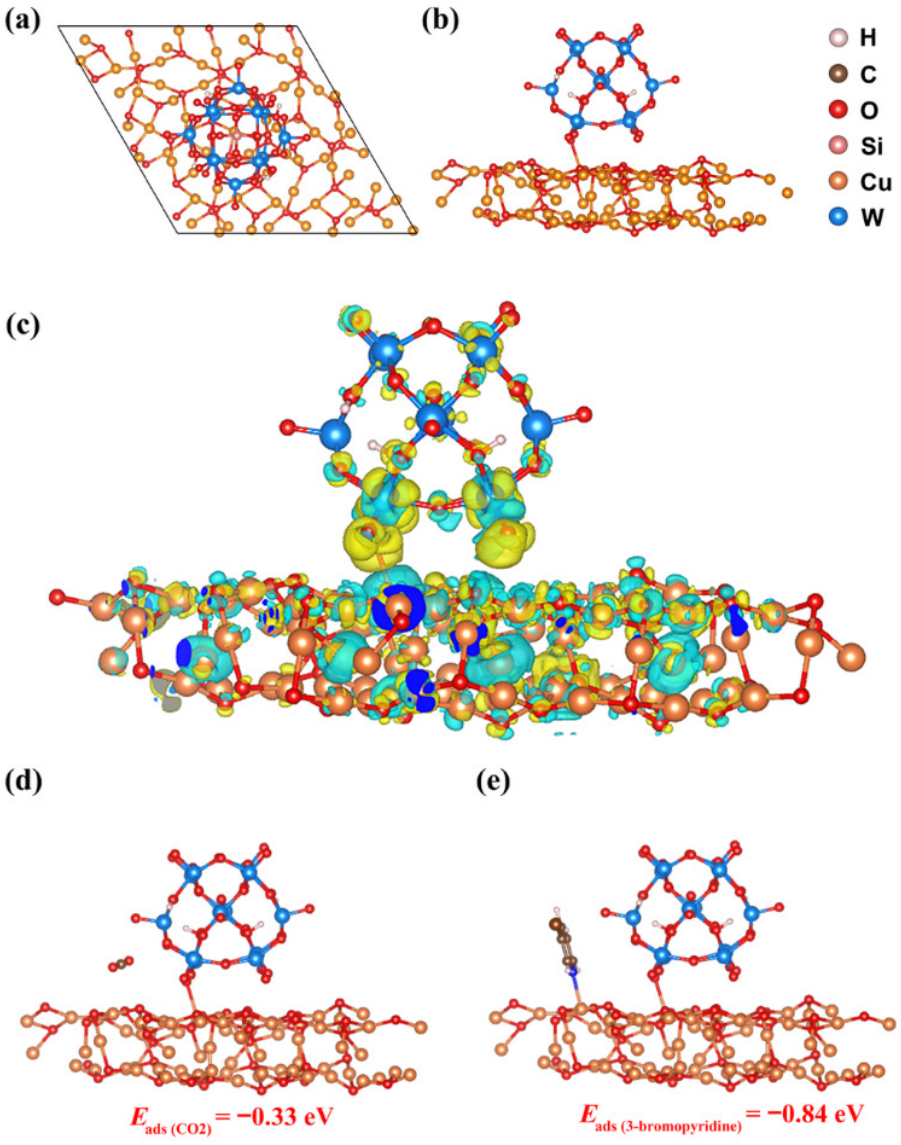

Figure 6 (a) Front and (b) side views of the optimized $SiW_{12}@Cu_2O$ structure. (c) Charge density difference of $SiW_{12}@Cu_2O$ with an isosurface level of 0.0008 e/Å^3. The cyan and yellow regions represent electron depletion and accumulation, respectively. Optimized adsorption configurations of (e) 3-bromopyridine and (d) CO_2 on the $SiW_{12}@Cu_2O$ surface.

integrity [65]. During the electrocatalytic conversion process, the dehalogenation of 3-bromopyridine (cleavage of the C–Br bond) is typically the rate-determining step, requiring the system to overcome a substantial energy barrier [66]. The high density of electrons accumulated on the SiW_{12} surface facilitates a more efficient electron injection into the C–Br antibonding orbitals of the adsorbed substrate. This significantly lowers the activation energy for reductive dehalogenation, accelerating the generation of active pyridyl radicals. Furthermore, this electron-rich environment enhances the activation capability toward electrophilic CO_2 molecules, promoting their bending deformation [67].

2. Substrate anchoring via Cu_2O sites

Second, the electron-deficient Cu_2O surface (indicated by the cyan regions in the figure) provides ideal substrate "anchoring" sites. Due to electron depletion, the Cu sites at the Cu_2O interface exhibit enhanced Lewis acidity, enabling specific Lewis acid–base interactions with the nitrogen (N) atoms of 3-bromopyridine molecules [68]. This Cu–N coordination interaction not only firmly adsorbs the substrate onto the electrode surface but also induces 3-bromopyridine to adopt a configuration favorable for the reaction, thereby maximizing the exposure of the C–Br sites to the adjacent POMs.

3. Dual-site synergistic C–C coupling

Finally, this "dual-site synergistic" mechanism significantly improves the efficiency of the critical C–C coupling step. The catalyst effectively constructs a confined reaction domain at the nanoscale: Cu_2O is responsible for capturing the "TBD-released" CO_2, whereas SiW_{12} facilitates the "cleavage" of bromine atoms and promotes CO_2 activation. This intimate interfacial contact ensures that the generated active pyridyl intermediates can undergo direct coupling reactions with activated CO_2 at the interface without the need for long-distance diffusion [69]. This synergistic effect substantially enhances the selectivity and yield of the high-value-added product, nicotinic acid.

To gain deeper insights into the interfacial reaction, we investigated the adsorption configurations of the reactants based on

the optimized SiW_{12}@Cu_2O model. The DFT calculations reveal distinct adsorption behaviors: 3-Bromopyridine exhibits strong chemisorption with an adsorption energy (E_{ads}) of −0.84 eV (Fig. 6(e)), primarily driven by the specific coordination between the pyridine nitrogen atom and the Lewis acidic Cu sites. This interaction induces a vertical "end-on" geometry that not only firmly anchors the substrate but also spatially orients the reactive C–Br bond toward the adjacent electron-rich SiW_{12} clusters. In contrast, CO_2 exhibits a moderate adsorption energy of −0.33 eV (Fig. 6(d)), indicating a metastable state that balances necessary surface activation with sufficient mobility for diffusion. This significant disparity in adsorption strengths validates a dual-site synergistic mechanism, where the electron-deficient Cu_2O surface serves as a specific "trap" for substrate immobilization, thereby facilitating efficient coupling with activated CO_2 within the confined interfacial domain constructed by SiW_{12}.

The experimental results and literature reports were considered together to reach the following conclusion (Fig. 7). The reaction mechanism proceeds through a coordinated sequence involving solution-phase CO_2 enrichment and surface-mediated radical coupling. Initially, the organic TBD base serves as a nucleophilic carrier in the CO_2 enrichment procedure (top panel), capturing bulk CO_2 to form a reactive zwitterionic TBD-CO_2 adduct. This step effectively concentrates and transports CO_2 to the electrode interface, after which the released TBD molecule allows subsequent adsorption of CO_2.

At the working electrode, which consists of SiW_{12}-anchored Cu_2O NPs (SiW_{12}@Cu NPs), concurrent electron transfer events occur. The 3-bromopyridine substrate undergoes reductive cleavage of the C–Br bond to yield a transient pyridyl radical (·Py) (as evidenced by *in situ* EPR spectra) [70–72] and a halide ion (X^-). Simultaneously, the released CO_2 is reduced to a CO_2 radical anion ($\cdot CO_2^-$) electrocatalyzed by the exposed Cu(I) active site [73–81]. The key C–C bond formation is then achieved via the C–C coupling of these two surface-bound species (indicated by the red dotted arrow), furnishing the nicotinate product. To maintain charge neutrality, the liberated halide ions migrate to the Pt counter electrode and undergo sacrificial oxidation to generate X_2.

Finally, to clarify the pivotal role of SiW_{12} in the catalyst system, composite catalysts with various SiW_{12} loadings were prepared by adjusting the SiW_{12}-to-$CuSO_4$ feed ratio. A systematic investigation into their catalytic reactivity was performed (Fig. S1 in the ESM). The results indicate that regulating the amount of SiW_{12} significantly alters the surface morphology of the catalyst. Subsequent yield analysis demonstrates that the catalytic reaction yield reaches its optimal level when the catalyst exhibits a cubic NP morphology. SiW_{12} modulates the morphological structure of the catalyst, in addition to regulating the electron transfer rate within the catalytic system. This is achieved through interaction with Cu atoms on the Cu NP surface. Consequently, the prepared catalyst exhibits excellent performance in the electrocatalytic dehalogenation of halogenated (hetero)aromatics, followed by direct carboxylation to CO_2.

4 Conclusions

In this study, a simple electrodeposition method was employed to load a specific amount of SiW_{12}@Cu NPs onto a CF surface. This approach facilitates the efficient carboxylation of halogenated electron-deficient aromatic heterocycles using CO_2 as a C1 feedstock under precious-metal-free conditions. Notably, this approach extends beyond halogenated aromatics, enabling efficient carboxylation of electron-deficient heterocycles, including pyridine rings, under mild conditions. Compared with conventional harsh methodologies, this strategy simplifies the carboxylation modification process for pharmaceutical intermediates and reduces the risk of structural damage to sensitive drug molecules. Furthermore, it enables the regulation of drug molecule properties, including water solubility, biological activity, and metabolic stability, through post-carboxylation modifications. Overall, these findings provide valuable technical support for molecular optimization and innovation in medicinal chemistry.

Electronic Supplementary Material: Supplementary material (SEM, CV, EIS, FT-IR, HPLC calibration curve, NMR spectra, etc.) is available in the online version of this article at https://doi.org/10.26599/POM.2026.9140126.

Data availability

All data needed to support the conclusions in the paper are presented in the manuscript and the Electronic Supplementary Material. Additional data related to this paper may be requested

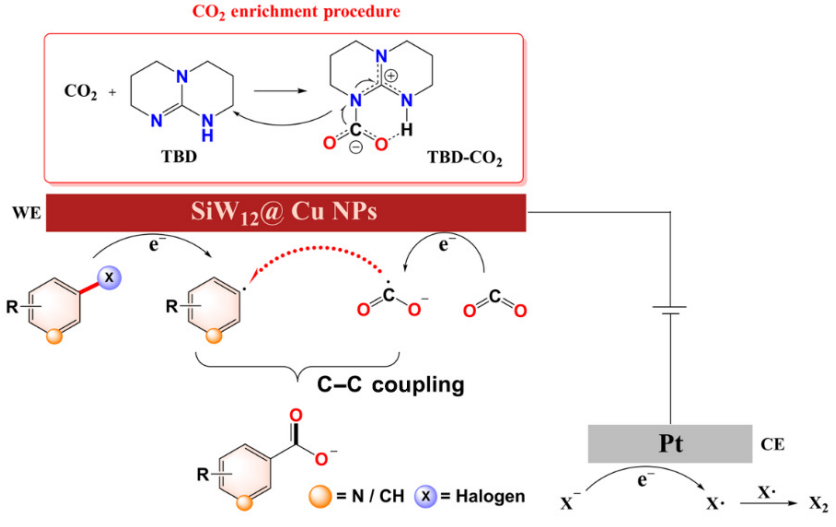

Figure 7 Proposed mechanism of electrocatalytic coupling of halo-(hetro)aromatic hydrocarbons and carbon dioxide.

from the corresponding author upon request.

Acknowledgements

The work was financially supported by the National Natural Science Foundation of China (No. 21801153), the Natural Science Foundation of Shandong Province (No. ZR2023MB065), the Joint Innovation Team for Clinical & Basic Research (No. 202401), the Scientific Research Project of Shandong Medical Association (No. YXH2024YS026), Science Research Project of Hebei Education Department (No. BJ2025145), and Scientific Research Program of Hebei University of Architecture (No. B-202409). We acknowledge Institute of Functional Material Chemistry, Northeast Normal University for providing the computational resources for this work.

Declaration of competing interest

All the contributing authors report no conflict of interests in this work.

Author contribution statement

T.-T. W.: Investigation, formal analysis, writing – original draft. C.-C. Z.: Model construction, theoretical calculation, analyzing. S.-Y. J.: Investigation, data curation. S.-J. Z.: Investigation, data curation. W.-Y. W. and M. Z.: Review. Y.-K. D.: Validation, funding acquisition. S. R.: Writing – review & editing, validation, supervision. B. L.: Review & editing, validation, supervision. Y. L. Y.: Methodology, writing – review & editing. D. J. Z.: Writing – review & editing, conceptualization, funding acquisition, supervision.

Use of AI statement

None.

References

[1] Wang, Y. W.; Zhao, Z. W.; Pan, D.; Wang, S. Y.; Jia, K. P.; Ma, D. K.; Yang, G. Q.; Xue, X. S.; Qiu, Y. A. Metal-free electrochemical carboxylation of organic halides in the presence of catalytic amounts of an organomediator. *Angew. Chem., Int. Ed.* **2022**, *61*, e202210201.

[2] Zang, D. J.; Wang, H. Q. Polyoxometalate-based nanostructures for electrocatalytic and photocatalytic CO_2 reduction. *Polyoxometalates* **2022**, *1*, 9140006.

[3] Zang, D. J.; Li, Q.; Dai, G. Y.; Zeng, M. Y.; Huang, Y. C.; Wei, Y. G. Interface engineering of Mo_8/Cu heterostructures toward highly selective electrochemical reduction of carbon dioxide into acetate. *Appl. Catal. B: Environ.* **2021**, *281*, 119426.

[4] Gautam, J.; Liu, Y.; Gu, J.; Ma, Z. Y.; Zha, J.; Dahal, B.; Zhang, L. N.; Chishti, A. N.; Ni, L. B.; Diao, G. W. et al. Fabrication of polyoxometalate anchored zinc cobalt sulfide nanowires as a remarkable bifunctional electrocatalyst for overall water splitting. *Adv. Funct. Mater.* **2021**, *31*, 2106147.

[5] Xia, S. M.; Chen, K. H.; Fu, H. C.; He, L. N. Ionic liquids catalysis for carbon dioxide conversion with nucleophiles. *Front. Chem.* **2018**, *6*, 462.

[6] Yang, C.; Hu, Y. R.; Li, S. X.; Huang, Q.; Peng, J. Self-supporting Bi–Sb bimetallic nanoleaf for electrochemical synthesis of formate by highly selective CO_2 reduction. *ACS Appl. Mater. Interfaces* **2023**, *15*, 6942–6950.

[7] Zheng, S. J.; Cheng, H.; Yu, J.; Bie, Q.; Chen, J. D.; Wang, F.; Wu, R.; Blackwood, D. J.; Chen, J. Three-dimensional ordered porous N-doped carbon-supported accessible Ni–N_x active sites for efficient CO_2 electroreduction. *Rare Met.* **2023**, *42*, 1800–1807.

[8] Luo, J. F.; Larrosa, I. C–H carboxylation of aromatic compounds through CO_2 fixation. *ChemSusChem* **2017**, *10*, 3317–3332.

[9] Gooßen, L. J.; Rodríguez, N.; Gooßen, K. Carboxylic acids as substrates in homogeneous catalysis. *Angew. Chem., Int. Ed.* **2008**, *47*, 3100–3120.

[10] Yang, D. S.; Yang, H. J.; Fu, H. Copper-catalyzed aerobic oxidative synthesis of aromatic carboxylic acids. *Chem. Commun.* **2011**, *47*, 2348–2350.

[11] Karpe, F.; Frayn, K. N. The nicotinic acid receptor-a new mechanism for an old drug. *Lancet* **2004**, *363*, 1892–1894.

[12] Zhao, Z. W.; Liu, Y.; Wang, S. Y.; Tang, S. Y.; Ma, D. K.; Zhu, Z. L.; Guo, C. C.; Qiu, Y. A. Site-selective electrochemical C–H carboxylation of arenes with CO_2. *Angew. Chem., Int. Ed.* **2023**, *62*, e202214710.

[13] Feng, L.; Wang, K. Y.; Day, G. S.; Ryder, M. R.; Zhou, H. C. Destruction of metal-organic frameworks: Positive and negative aspects of stability and lability. *Chem. Rev.* **2020**, *120*, 13087–13133.

[14] Sun, G. Q.; Liao, L. L.; Ran, C. K.; Ye, J. H.; Yu, D. G. Recent advances in electrochemical carboxylation with CO_2. *Acc. Chem. Res.* **2024**, *57*, 2728–2745.

[15] König, M.; Lin, S. H.; Vaes, J.; Pant, D.; Klemm, E. Integration of aprotic CO_2 reduction to oxalate at a Pb catalyst into a GDE flow cell configuration. *Faraday Discuss.* **2021**, *230*, 360–374.

[16] Sun, G. Q.; Zhang, W.; Liao, L. L.; Li, L.; Nie, Z. H.; Wu, J. G.; Zhang, Z.; Yu, D. G. Nickel-catalyzed electrochemical carboxylation of unactivated aryl and alkyl halides with CO_2. *Nat. Commun.* **2021**, *12*, 7086.

[17] Ye, B. H.; Su, L.; Zheng, K. T.; Gao, S.; Liu, J. W. Synergistic photoredox/palladium catalyzed enantioconvergent carboxylation of racemic heterobiaryl (pseudo)halides with CO_2. *Angew. Chem., Int. Ed.* **2025**, *64*, e202413949.

[18] Liu, G.; Zhang, H. J.; Kang, J. X.; Guo, L. Electrocatalytic materials engineering: Towards the renaissance of electrochemical organic synthesis. *Mater. Today* **2025**, *87*, 422–441.

[19] Xie, S. L.; Gao, X. T.; Wu, H. H.; Zhou, F.; Zhou, J. Direct electrochemical defluorinative carboxylation of *gem*-difluoroalkenes with carbon dioxide. *Org. Lett.* **2020**, *22*, 8424–8429.

[20] Zhu, C. J.; Ang, N. W. J.; Meyer, T. H.; Qiu, Y. A.; Ackermann, L. Organic electrochemistry: Molecular syntheses with potential. *ACS Cent. Sci.* **2021**, *7*, 415–431.

[21] Cheng, X.; Lei, A. W.; Mei, T. S.; Xu, H. C.; Xu, K.; Zeng, C. C. Recent applications of homogeneous catalysis in electrochemical organic synthesis. *CCS Chem.* **2022**, *4*, 1120–1152.

[22] Tang, S. B.; Liu, Z. Z.; Zhang, J. K.; Li, B.; Wang, B. Q. Copper-catalyzed C4-selective carboxylation of pyridines with CO_2 via pyridylphosphonium salts. *Angew. Chem., Int. Ed.* **2024**, *63*, e202318572.

[23] Bodor, E. T.; Offermanns, S. Nicotinic acid: An old drug with a promising future. *Br. J. Pharmacol.* **2008**, *153*, S68–S75.

[24] Carlson, L. A. Nicotinic acid: The broad-spectrum lipid drug. A 50th anniversary review. *J. Intern. Med.* **2005**, *258*, 94–114.

[25] Uebanso, T.; Shimohata, T.; Mawatari, K.; Takahashi, A. Functional roles of B-vitamins in the gut and gut microbiome. *Mol. Nutr. Food Res.* **2020**, *64*, 2000426.

[26] Hu, Q. L.; Li, K.; Chen, X. J.; Liu, Y. F.; Yang, G. P. Polyoxometalate catalysts for the synthesis of N-heterocycles. *Polyoxometalates* **2024**, *3*, 9140048.

[27] Zhang, Q.; Li, F. Y.; Xu, L. Application of polyoxometalates in third-generation solar cells. *Polyoxometalates* **2023**, *2*, 9140018.

[28] Xia, Z. N.; Wang, L. B.; Zhang, Q.; Li, F. Y.; Xu, L. Fast degradation of phenol over porphyrin-polyoxometalate composite photocatalysts under visible light. *Polyoxometalates* **2022**, *1*, 9140001.

[29] Sun, J. Y.; Wang, Z. L.; Zhang, Z.; Liu, G. C.; Wang, X. L. Hydrothermal synthesis, structure, and catalytic properties of a (4,6)-connected framework constructed from Keggin-type polyoxometalate units and tetranuclear copper complexes. *Polyoxometalates* **2024**, *3*, 9140039.

[30] Ni, Z. H.; Liu, N.; Zhao, C. H.; Mi, L. Hexanuclear nickel-added silicotungstates as high-efficiency electrocatalysts for nitrate reduction to ammonia. *Polyoxometalates* **2024**, *3*, 9140044.

[31] Yang, G. P.; Lin, Z. F.; Zhang, X. Z.; Cao, J. W.; Chen, X. J.; Liu, Y. F.; Lin, X. L.; Li, K. Assembly of Y(III)-containing antimonotungstates induced by malic acid with catalytic activity for the synthesis of imidazoles. *Chin. Chem. Lett.* **2024**, *35*, 110274.

[32] Yang, G. P.; Liu, H. Q.; Chen, J. C.; Lin, X. L.; Tan, K. X.; Dong, Y. Y.; Liu, Y. F.; Wei, Y. G. Dy/Ho-encapsulated tartaric acid-functionalized tungstoantimonates: Heterogeneous catalysts for isoindolinone synthesis. *Chem. Commun.* **2024**, *60*, 10934–10937.

[33] Zang, D. J.; Huang, Y. C.; Li, Q.; Tang, Y. J.; Wei, Y. G. Cu dendrites induced by the Anderson-type polyoxometalate $NiMo_6O_{24}$ as a promising electrocatalyst for enhanced hydrogen evolution. *Appl. Catal. B: Environ.* **2019**, *249*, 163–171.

[34] Guo, L.; He, L.; Zhuang, Q. H.; Li, B. L.; Wang, C. F.; Lv, Y. F.; Chu, J. F.; Song, Y. F. Recent advances in confining polyoxometalates and the applications. *Small* **2023**, *19*, 2207315.

[35] Wang, Z. M.; Xin, X.; Zhang, M.; Li, Z.; Lv, H. J.; Yang, G. Y. Recent advances of mixed-transition-metal-substituted polyoxometalates. *Sci. China Chem.* **2022**, *65*, 1515–1525.

[36] Lee, H. J.; Cho, E. S. Selective photocatalytic C–C bond cleavage of lignin models and conversion to high-value chemical by polyoxometalate under a mild water-based environment. *ACS Sustainable Chem. Eng.* **2023**, *11*, 7624–7632.

[37] Chen, L.; Chen, W. L.; Wang, X. L.; Li, Y. G.; Su, Z. M.; Wang, E. B. Polyoxometalates in dye-sensitized solar cells. *Chem. Soc. Rev.* **2019**, *48*, 260–284.

[38] Cheng, Y.; Qin, K. J.; Zang, D. J. Polyoxometalates based nanocomposites for bioapplications. *Rare Met.* **2023**, *42*, 3570–3600.

[39] Yue, K. H.; Lu, R. H.; Gao, M. B.; Song, F.; Dai, Y.; Xia, C. F.; Mei, B. B.; Dong, H. L.; Qi, R. J.; Zhang, D. L. et al. Polyoxometalated metal-organic framework superstructure for stable water oxidation. *Science* **2025**, *388*, 430–436.

[40] Coronado, E.; Gómez-García, C. J. Polyoxometalate-based molecular materials. *Chem. Rev.* **1998**, *98*, 273–296.

[41] Liu, J. X.; Zhang, X. B.; Li, Y. L.; Huang, S. L.; Yang, G. Y. Polyoxometalate functionalized architectures. *Coord. Chem. Rev.* **2020**, *414*, 213260.

[42] Ru, S.; Zhao, C. C.; Wu, Z. K.; Yan, L. K.; Zang, D. J.; Wei, Y. G. Molecular photocatalysts based on quinolinium-grafted polyoxometalates for efficient one-step aerobic oxidation of benzyl alcohols to benzoic acids. *ACS Sustainable Chem. Eng.* **2024**, *12*, 6827–6839.

[43] Wang, F. Q.; Zhang, Y.; Wang, W. W.; Fu, M. Q.; Mo, H. B.; Yu, W. D.; Liu, C.; Yan, J. Discovery of a new family member of arsenic-vanadium polyoxometalates with high catalytic performance for one-pot coupling of CO_2, epoxides and amines. *Tungsten* **2025**, *7*, 80–87.

[44] Dashtian, K.; Shahsavarifar, S.; Usman, M.; Joseph, Y.; Ganjali, M. R.; Yin, Z. Y.; Rahimi-Nasrabadi, M. A comprehensive review on advances in polyoxometalate based materials for electrochemical water splitting. *Coord. Chem. Rev.* **2024**, *504*, 215644.

[45] Gumerova, N. I.; Rompel, A. Synthesis, structures and applications of electron-rich polyoxometalates. *Nat. Rev. Chem.* **2018**, *2*, 0112.

[46] Bagheri, A. R.; Aramesh, N.; Chen, J. B.; Liu, W. N.; Shen, W.; Tang, S.; Lee, H. K. Polyoxometalate-based materials in extraction, and electrochemical and optical detection methods: A review. *Anal. Chim. Acta* **2022**, *1209*, 339509.

[47] Kaufman, Y.; Neumann, R. Copper-substituted polyoxotungstates as catalysts for the electrocatalytic oxygenation of light alkanes. *Inorg. Chem.* **2025**, *64*, 18365–18375.

[48] Gomey, S.; Raula, M.; Gupta, U.; Mahata, A.; Bhattacharyya, K.; Sengupta, S.; Chakraborty, B. Cu_2O NPs as visible-light photosensitizer impregnated on self-doped TiO_2–$PTiW_{11}O_{40}$ p-n heterojunctions for photo-, electro-, and photoelectrochemical hydrogen production. *ACS Appl. Nano Mater.* **2025**, *8*, 22965–22976.

[49] Jiang, Q. S.; Wang, X. M.; Li, G.; Zhao, N.; Pang, H. J.; Ma, H. Y. Single-site polyoxometalate complexes with engineered electron channels for efficient electrocatalytic ammonia synthesis from nitrate. *Small* **2025**, *21*, e09113.

[50] Li, X.; Hui, H. H.; Ren, Y. H.; Liu, Z. Q.; Li, Y. Y.; Yue, B.; He, H. Y.; Tsang, S. C. E. Switchable high-valent Ag^{3+}/Ag^{+} redox pair stabilized in polyoxometalate as highly oxidative "electron shuttle" catalysts. *JACS Au* **2025**, *5*, 5089–5097.

[51] Anyushin, A. V.; Kondinski, A.; Parac-Vogt, T. N. Hybrid polyoxometalates as post-functionalization platforms: From fundamentals to emerging applications. *Chem. Soc. Rev.* **2020**, *49*, 382–432.

[52] Kresse, G.; Hafner, J. *Ab initio* simulation of the metal/nonmetal transition in expanded fluid mercury. *Phys. Rev. B* **1997**, *55*, 7539–7548.

[53] Perdew, J. P.; Chevary, J. A.; Vosko, S. H.; Jackson, K. A.; Pederson, M. R.; Singh, D. J.; Fiolhais, C. Atoms, molecules, solids, and surfaces: Applications of the generalized gradient approximation for exchange and correlation. *Phys. Rev. B* **1992**, *46*, 6671–6687.

[54] Perdew, J. P.; Burke, K.; Ernzerhof, M. Generalized gradient approximation made simple. *Phys. Rev. Lett.* **1996**, *77*, 3865–3868.

[55] Grimme, S. Semiempirical GGA-type density functional constructed with a long-range dispersion correction. *J. Comput. Chem.* **2006**, *27*, 1787–1799.

[56] Nørskov, J. K.; Rossmeisl, J.; Logadottir, A.; Lindqvist, L.; Kitchin, J. R.; Bligaard, T.; Jónsson, H. Origin of the overpotential for oxygen reduction at a fuel-cell cathode. *J. Phys. Chem. B* **2004**, *108*, 17886–17892.

[57] Kim, Y. G.; Baricuatro, J. H.; Javier, A.; Gregoire, J. M.; Soriaga, M. P. The evolution of the polycrystalline copper surface, first to Cu(111) and then to Cu(100), at a fixed CO_2RR potential: A study by *operando* EC-STM. *Langmuir* **2014**, *30*, 15053–15056.

[58] Berry, F. J.; Derrick, G. R.; Mortimer, M. Identification and characterisation of stable phases of silicotungstic acid, $H_4SiW_{12}O_{40}{\cdot}nH_2O$. *Polyhedron* **2014**, *68*, 17–22.

[59] Chu, W. L.; Yang, X. G.; Shan, Y. K.; Ye, X. K.; Wu, Y. Immobilization of the heteropoly acid (HPA) $H_4SiW_{12}O_{40}$ (SiW_{12}) on mesoporous molecular sieves (HMS and MCM-41) and their catalytic behavior. *Catal. Lett.* **1996**, *42*, 201–208.

[60] Yan, H. J.; Tian, C. G.; Sun, L.; Wang, B.; Wang, L.; Yin, J.; Wu, A. P.; Fu, H. G. Small-sized and high-dispersed WN from $[SiO_4(W_3O_9)_4]^{4-}$ clusters loading on GO-derived graphene as promising carriers for methanol electro-oxidation. *Energy Environ. Sci.* **2014**, *7*, 1939–1949.

[61] Guillén-López, A.; Espinosa-Torres, N. D.; Cuentas-Gallegos, A. K.; Robles, M.; Muñiz, J. Understanding bond formation and its impact on the capacitive properties of SiW12 polyoxometalates adsorbed on functionalized carbon nanotubes. *Carbon* **2018**, *130*, 623–635.

[62] Yu, H. H.; Wei, B.; Wang, J. P.; Zhao, H. Q.; Zeng, S.; Xue, C. B.; Zhu, J. Y.; Zhang, Y. L.; Xu, P. Facile synthesis, characterization, mechanism and enhanced visible-light photocatalytic activity of SiW_{12}/α-Fe_2O_3 nanocomposites. *New J. Chem.* **2021**, *45*, 10063–10069.

[63] Kholdeeva, O. A.; Maksimchuk, N. Y.; Maksimov, G. M. Polyoxometalate-based heterogeneous catalysts for liquid phase

selective oxidations: Comparison of different strategies. *Catal. Today* **2010**, *157*, 107–113.

[64] Weinstock, I. A.; Schreiber, R. E.; Neumann, R. Dioxygen in polyoxometalate mediated reactions. *Chem. Rev.* **2018**, *118*, 2680–2717.

[65] Pope, M. T.; Müller, A. Polyoxometalate chemistry: An old field with new dimensions in several disciplines. *Angew. Chem., Int. Ed.* **1991**, *30*, 34–48.

[66] Costentin, C.; Robert, M.; Savéant, J. M. Catalysis of the electrochemical reduction of carbon dioxide. *Chem. Soc. Rev.* **2013**, *42*, 2423–2436.

[67] Nitopi, S.; Bertheussen, E.; Scott, S. B.; Liu, X. Y.; Engstfeld, A. K.; Horch, S.; Seger, B.; Stephens, I. E. L.; Chan, K.; Hahn, C. et al. Progress and perspectives of electrochemical CO_2 reduction on copper in aqueous electrolyte. *Chem. Rev.* **2019**, *119*, 7610–7672.

[68] Tortajada, A.; Juliá-Hernández, F.; Börjesson, M.; Moragas, T.; Martin, R. Transition-metal-catalyzed carboxylation reactions with carbon dioxide. *Angew. Chem., Int. Ed.* **2018**, *57*, 15948–15982.

[69] Wang, W.; Deng, C. Y.; Xie, S. J.; Li, Y. F.; Zhang, W. Y.; Sheng, H.; Chen, C. C.; Zhao, J. C. Photocatalytic C–C coupling from carbon dioxide reduction on copper oxide with mixed-valence copper(I)/copper(II). *J. Am. Chem. Soc.* **2021**, *143*, 2984–2993.

[70] Lan, J. P.; Yu, W. J.; You, K.; Xu, M. Y.; Zhang, B.; Wang, Y. Q.; Wang, T.; Luo, J. Dehalogenative arylation of unactivated alkyl halides via electroreduction. *Org. Lett.* **2023**, *25*, 7434–7439.

[71] Zhao, Z. F.; Yao, X. Y.; Zhang, L. L.; Yu, R. P.; Xu, Y. H.; Chu, Y. Q.; Mao, X. B.; Zheng, H. J. Electrocatalytic dehalogenation in the applications of organic synthesis and environmental degradation. *EcoEnergy* **2024**, *2*, 83–113.

[72] Guo, Y.; Li, Y.; Wang, Z. W. Electrocatalytic hydro-dehalogenation of halogenated organic pollutants from wastewater: A critical review. *Water Res.* **2023**, *234*, 119810.

[73] Zhang, S.; Fan, Q.; Xia, R.; Meyer, T. J. CO_2 reduction: From homogeneous to heterogeneous electrocatalysis. *Acc. Chem. Res.* **2020**, *53*, 255–264.

[74] Nam, D. H.; De Luna, P.; Rosas-Hernández, A.; Thevenon, A.; Li, F. W.; Agapie, T.; Peters, J. C.; Shekhah, O.; Eddaoudi, M.; Sargent, E. H. Molecular enhancement of heterogeneous CO_2 reduction. *Nat. Mater.* **2020**, *19*, 266–276.

[75] Li, Y.; Guan, B.; Zhuang, Z. Q.; Chen, J. Y.; Zhu, L.; Ma, Z. R.; Hu, X. H.; Zhu, C. Y.; Shu, S. K.; Dang, H. T. et al. Optimization strategies for electrocatalytic CO_2 reduction based on atomically dispersed copper: A review. *Adv. Funct. Mater.* **2025**, *35*, 2417732.

[76] Saha, P.; Amanullah, S.; Dey, A. Selectivity in electrochemical CO_2 reduction. *Acc. Chem. Res.* **2022**, *55*, 134–144.

[77] Xu, S. Z.; Carter. E. A. Theoretical insights into heterogeneous (photo)electrochemical CO_2 reduction. *Chem. Rev.* **2019**, *119*, 6631–6669.

[78] Cheng, Y.; Zhao, C. C.; Wang, T. T.; Zhang, M.; Ru, S.; Deng, Y. K.; Wang, W. Y.; Wang, Y.; Song, Y.; Wei, Y. et al. Interfacial engineering of Cu_9S_5@MoS_2 p-n type heterojunction via *in situ* phase separation for highly efficient electrocatalytic oxidation of 5-hydroxymethylfurfural. *eScience*, in press, DOI: 10.1016/j.esci.2025.100507.

[79] Xiao, W.; Zhang, J.; Wu, J. Recent advances in reactions involving carbon dioxide radical anion. *ACS Catal.* **2023**, *13*, 15991–16011.

[80] Alkayal, A.; Tabas, V.; Montanaro, S.; Wright, I. A.; Malkov, A. V.; Buckley, B. R. Harnessing applied potential: Selective β-hydrocarboxylation of substituted olefins. *J. Am. Chem. Soc.* **2020**, *142*, 1780–1785.

[81] Sheta, A. M.; Alkayal, A.; Mashaly, M. A.; Said, S. B.; Elmorsy, S. S.; Malkov, A. V.; Buckley, B. R. Selective electrosynthetic hydrocarboxylation of α,β-unsaturated esters with carbon dioxide. *Angew. Chem., Int. Ed.* **2021**, *60*, 21832–21837.

Teng-Teng Wang is currently a master's student in the group of Prof. Dejin Zang at Shandong First Medical University. Her research focuses on photo- and electrocatalytic green synthesis of pharmaceutical molecules based on polyoxometalate clusters. She has published 5 academic papers, including 3 as first/co-first author in SCI journals: *Chin. Chem. Lett.*, *Polyoxometalates*, and *Nano Res*.

Cong-Cong Zhao received Ph.D. degree in Physical Chemistry from Northeast Normal University in 2024. Currently, she is a Lecturer in the Department of Mathematics and Physics, Hebei University of Architecture. Her research focuses on the mechanism study of polyoxometalates and two-dimensional materials in a series of electro- and photo-catalytic reactions including CO2RR/NRR. She is the principal investigator of one Hebei Province Young Top-Notch Talent Project and has participated in several research projects, including the General Program of the National Natural Science Foundation of China and projects supported by the Department of Education of Hebei Province. Currently, she has published 15 SCI papers as first author (co-first author) in journals including *eScience*, *Adv. Funct. Mater.*, *Chinese J Catal.*, and *J. Mater. Chem. A*.

Liu Bin is an Associate Chief Physician at the Third Affiliated Hospital of Shandong First Medical University. He earned his Master's degree in Internal Medicine of Traditional Chinese Medicine (Oncology) from Nanjing University of Chinese Medicine in 2010. His research focuses on comprehensive internal medicine treatment of common malignancies, including lung cancer and colorectal cancer. He also possesses specialized insights in palliative care and physician-patient communication.

Shi Ru received his Ph.D. degree in Chemistry from Tsinghua University in 2024. Currently, he is a postdoctoral researcher in the research group of Prof. Dejin Zang at the School of Pharmacy, Shandong First Medical University. His research focuses on the design, synthesis, and application of polyoxometalate-based photo catalysts. He has participated in the General Program of the National Natural Science Foundation of China and has published 14 SCI papers, including 6 as first author (co-first author) in high-impact journals: *Angew. Chem.*, *Int. Ed.* (2), *Green Chem.* (1), *ACS Sustainable Chem. Eng.* (1), *ChemCatChem* (1), and *Nano Res.* (1).

Yulv Yu is a Senior Scientist at the Chambroad Institute. He received his Ph.D. from Peking University in 2018, after which he served as a postdoctoral researcher at the same institution. Dr. Yu was an associate research fellow at Peking University from 2021 to 2024. His primary research interest lies in the catalytic conversion of C1 molecules.

Dejin Zang is an Associate Professor at Shandong First Medical University & Shandong Academy of Medical Sciences. He earned his Ph.D. from the University of Strasbourg in 2017 under the supervision of Prof. Laurent Ruhlmann, after that, he served as a post-doctor in Tsinghua university under the supervision of Prof. Yongge Wei. He established his independent research group in 2021. His research primarily focuses on the development of polyoxometalate-based functional materials and catalytic chemistry, with particular emphasis on biomass conversion, green synthesis of pharmaceutical intermediates, and the development of novel boron neutron capture therapy (BNCT) agents.